A new potential function for the calculation of contact forces in the combined finite–discrete element method

C.Z. Yan[1,2] and H. Zheng[2,*,†]

[1]*State Key Laboratory of Geomechanics and Geotechnical Engineering, Institute of Rock and Soil Mechanics, Chinese Academy of Sciences, Wuhan 430071, China*
[2]*Key Laboratory of Urban Security and Disaster Engineering (Beijing University of Technology), Ministry of Education, Beijing 100124, China*

SUMMARY

Although the potential contact force proposed by Munjiza overcomes the difficulties inherent in the traditional discrete element methods, the physical meaning of the potential is not clear and the contact force derived from the original potential function is strongly dependent on the mesh configuration. In this study, we redefine a potential function and propose a new contact force calculation method based on a unified standard. Moreover, the new potential function retains all the advantages of the original potential function but has less mesh dependency. Copyright © 2016 John Wiley & Sons, Ltd.

1. INTRODUCTION

The rupture phenomenon of brittle rock has been a hot spot of experimental and theoretical studies. Many problems in rock mechanics and rock engineering are related to the rock fracture closely.

Some knowledge of complex rock fracture has been accumulated based on experimental observations [1–4]. However, the mechanisms related to rock fracture, such as a crack initiation and propagation, remain unclear owing to huge difficulties in tracking crack initiation and propagation during experiment [5]. Classic fracture mechanics is another means to study rock fracture. In most of the literature, research is limited to a single crack [6, 7] or a small number of cracks [8]. Thus, classic fracture mechanics is hard to deal with the propagation or interference of multiple cracks in rock mass [9].

There are some numerical methods for studying multiple crack propagation [5, 10, 11]. For example, Tang [10] proposed the rock failure process analysis system based on the finite element method together with the material rupture algorithm, which can simulate crack initiation, propagation, and intersection. Later, Liang *et al.* [5, 11] conducted a three-dimensional numerical simulation of rock fracture. Potyondy and Cundall [12] proposed a bonded particle model, which reproduced many mechanic characteristics of rocks, including elasticity, fracture, acoustic emission, material anisotropy caused by cumulative damage, dilatancy, softening, and strength increase with increased confining pressure.

---

*Correspondence to: H. Zheng, State Key Laboratory of Geomechanics and Geotechnical Engineering, Institute of Rock and Soil Mechanics, Chinese Academy of Sciences, Wuhan 430071, China.
†E-mail: hzheng@whrsm.ac.cn

In addition, Munjiza proposed the combined finite–discrete element method (FDEM) to simulate continuum fracture and obtained some good results [13–16]. In FDEM, a continuum is discretized as a mesh consisting of triangular solid elements and joint elements with cohesive behaviors. The movement of each triangular solid element is determined by the imbalance force acting on the triangular solid elements, which is similar to the discrete element method (DEM). By the breakage of joint elements, the crack initiation and propagation in the rock mass are simulated [17]. Before fracture, the deformation of continuum can be represented by those solid elements and joint elements. This method has some advantages over the particle flow method in simulating rock fracture, such as the following aspects: there is no gap between solid elements in the initial model, solid elements are deformable, and the concepts of stress and strain in continuum are well preserved.

Another important advantage of FDEM over the DEM is that the contact force in FDEM is defined as a distributed load, leading contact to less stress concentration [18]. Unlike DEM, where the angle-to-angle contact needs to be round to avoid stress concentration [19, 20], the calculation of contact forces in FDEM does not need any special treatment. Many scholars studied the calculation of contact force. For example, Lankarani *et al.* [21] and Elata *et al.* [22] proposed contact force models in classical contact mechanics. In computational mechanics of discontinua, Renzo and Miao [23] compared different contact-force models in DEM-based granular flow codes. Choi *et al.* [24] presented a general purpose contact algorithm using a compliance contact force model. In computational mechanics of continua, Wang *et al.* [25] proposed a contact force algorithm that satisfies the condition of no-penetration accurately. Willam *et al.* [26] proposed an interface damage model for thermomechanical degradation of heterogeneous materials. Caballero *et al.* [27] presented a consistent tangent formulation for 3D interface modeling of cracking/fracture in quasi-brittle materials. Xuan *et al.* [28] proposed an entropy-based evaluation of contact forces in continuum mechanics.

It is worth noting that Munjiza *et al.* [14] presented contact force calculation between all kinds of basic geometric shapes in detail. Moreover, they proposed a contact force calculation method based on potential in FDEM [18]. Although the potential contact force in FDEM avoids the difficulty of DEM in the treatment of angle-to-angle contacts, the physical meaning of the potential is not very clear. For example, the magnitude of the contact force is very dependent on the shape and size of the elements in contact, which will be seen subsequently.

In this study, we redefine the potential function based on a unified standard, which retains all the advantages of the original potential definition. By this new potential function, the contact forces for the same contact embedding are equal, which makes the crack path closer to the theoretical solution than those by the original potential function.

2. FDEM FUNDAMENTALS

From the perspective of code implementation, a calculation loop of FDEM can be divided into the following steps.

1. Contact detection.
2. Calculation of contact forces.
3. Calculation of node forces caused by deformation of triangular solid elements.
4. Calculation of node forces caused by deformation of joint elements and determination of new joint elements fractured.
5. Time integration to update the coordinate of the triangular element nodes.

Next, we briefly describe each aforementioned step, but the second step will be described in detail in Section 3 in that it is the core of this study.

2.1. Contact detection

Initially, the no binary search (NBS) algorithm proposed by Munjiza [29] is used to contact detection in FDEM. The time consumption of NBS is linear with the number of elements. For the mesh having

solid elements with nearly equal size, the efficiency of contact detection is very high. However, the memory consumption of NBS is dependent on the packing density of solid element. Thus, Munjiza *et al.* [30] proposed the Munjiza–Rougier algorithm, which has insignificant CPU and memory requirements that are independent of spatial distribution of solid element.

The basic process of both NBS and Munjiza–Rougier algorithms is stated as follows. First, the spatial domain is divided into a square grid with the cell edge length equal to the maximum diameter of the circumscribed circle of all the triangular solid elements. Then all the triangular solid elements are mapped into the corresponding cells according to the center coordinates of these triangular elements. This process is shown in Figure 1; black dots represent the center of a triangular element. The cell at which a triangular solid element center is located can be calculated by

$$\left. \begin{array}{l} m = 1 + \text{INT}\left(\dfrac{x_c - x_{\min}}{d}\right) \\[2mm] n = 1 + \text{INT}\left(\dfrac{y_c - y_{\min}}{d}\right) \end{array} \right\}, \tag{1}$$

where x_c and y_c are the center coordinates of the triangular element; n and m represent the row number and the column number, respectively; and INT() is the rounded-down function.

After the aforementioned mapping, the following process is carried out. Take Figure 2 as an example, where the center of element 1 is in the target cell. If we want to know whether there are other elements in contact with element 1, we only need to determine if there are element centers in the target cell or the eight adjacent cells around the target cell. Owing to the symmetry of duplicate determination, actually, we only need to determine whether there are element centers in the five cells as shown in Figure 2. Thus, the efficiency of contact detection improves markedly.
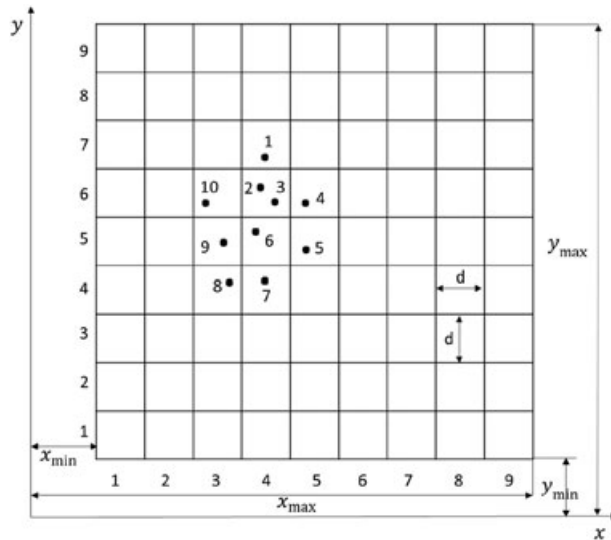

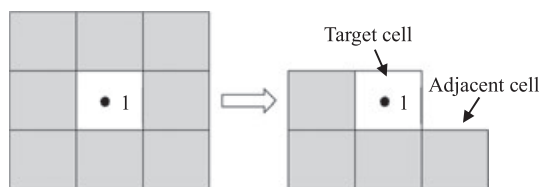Figure 1. Mapping triangular elements into the space cells.

Figure 2. Target cell and adjacent cells in detection.

2.2. Node force caused by deformation of triangular elements

In FDEM, the solid domain of interest is meshed into a series of triangular solid elements, and the deformation and stress of a single solid element are calculated by a large strain–large displacement formulation for the finite element side of FDEM. Recently, this formulation has been generalized through the concept of the so-called Munjiza material element [31]. For homogeneous and isotropic materials, the constitutive relation is given by [13]

$$\mathbf{T} = \frac{1}{\sqrt{|\det\mathbf{F}|}} \left[\frac{E}{1+v} \mathbf{E}_d + \frac{E}{1-v} \mathbf{E}_s + 2\mu\mathbf{D} \right], \tag{2}$$

where $\mathbf{T}$ is the stress tensor in the overall coordinate after element deformation; $\mathbf{F}$ is deformation gradient; $\mathbf{E}_d$ and $\mathbf{E}_s$ are Green and St. Venant strain tensors due to the shape and volume change, respectively; E and v are Young's modulus and Poisson's ratio, respectively; μ is viscous damping coefficient; and $\mathbf{D}$ is the strain rate tensor. As triangular solid elements in FDEM yield constant strains, the equivalent nodal force of each edge caused by deformation of triangular elements can be calculated by

$$\mathbf{f}_n = \frac{1}{2}\mathbf{T}\mathbf{n}l = \frac{1}{2} \begin{bmatrix} \sigma_{xx} & \sigma_{xy} \\ \sigma_{yx} & \sigma_{yy} \end{bmatrix} \begin{bmatrix} n_x \\ n_y \end{bmatrix} l, \tag{3}$$

where $\mathbf{n}$ is the unit outward normal vector of the triangular element edge and l is length of the triangular element edge.

2.3. Fracture model of joint elements

As shown in Figure 3, joint elements in FDEM are assumed to have cohesive behaviors. The stress–displacement relationship of a typical joint element is based on the combined single and smeared crack model [17]. Through the breakage of joint elements, the crack initiation and propagation are simulated. As a consequence, the crack propagation is only along the edges of the triangular solid elements.

As shown in Figure 4, the four nodes of a joint element are marked by N_i ($i = 1, 2, 3, 4$). Initially, there is no gap between the two edges of the joint element, that is to say, point N coincides with point N'. If the joint element is open, the open vector at the point is given by

$$\boldsymbol{\delta} = \mathbf{p}_N - \mathbf{p}_{N'}, \tag{4}$$

where $\mathbf{p}_N$ and $\mathbf{p}_{N'}$ are the position vectors of points N and N', respectively.

The open vector $\boldsymbol{\delta}$ of a point on the center line of the joint element can be divided as follows:

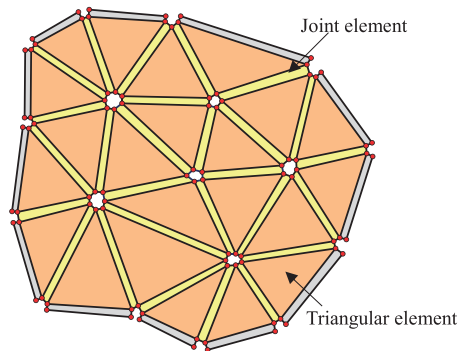$$\boldsymbol{\delta} = \delta_n\mathbf{n} + \delta_t\mathbf{t}, \tag{5}$$

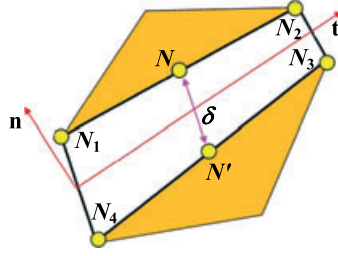Figure 3. Mesh topology in combined finite–discrete element method.

Figure 4. Schematic of opening in a joint element.

where δ_n and δ_t are the normal and tangential components of the open vector $\boldsymbol{\delta}$, namely, the normal opening amount and tangential slippage amount; and $\mathbf{n}$ and $\mathbf{t}$ are unit vectors in the normal direction and tangential direction of the middle line in the joint element, respectively. The two unit vectors can be expressed by

$$t = \frac{\dfrac{(\mathbf{p}_{N_2} + \mathbf{p}_{N_3})}{2} - \dfrac{(\mathbf{p}_{N_1} + \mathbf{p}_{N_4})}{2}}{\left| \dfrac{(\mathbf{p}_{N_2} + \mathbf{p}_{N_3})}{2} - \dfrac{(\mathbf{p}_{N_1} + \mathbf{p}_{N_4})}{2} \right|}. \tag{6}$$

$$\mathbf{n} = \boldsymbol{\delta} - (\boldsymbol{\delta} \cdot \mathbf{t})\mathbf{t}$$

Thus, the normal opening amount and tangential slippage amount can be expressed as

$$\begin{aligned} \delta_{\mathrm{n}} &= \boldsymbol{\delta} \cdot \mathbf{n} \\ \delta_{\mathrm{t}} &= \boldsymbol{\delta} \cdot \mathbf{t}. \end{aligned} \tag{7}$$

Similarly, the bonding stress vector of the joint element can be also decomposed into

$$\boldsymbol{T} = \sigma\mathbf{n} + \tau\mathbf{t}, \tag{8}$$

where σ and τ are normal and tangential stress components of the bonding stress vector.

The key point is to build a proper relationship between the bonding stress components and the displacement components of the joint element. Munjiza proposed a combined single and smeared crack model to describe the relationship (Figure 5).

In Figure 5(a), δ_{nt} is the normal opening amount of the joint element when the crack tip reaches the tensile strength f_t. In theory, the normal opening amount of the crack is zero if the normal bonding stress is lower than the tensile strength f_t. However, as the penalty method is used, the normal opening amount of the joint element at this moment is not zero but $\delta = \delta_{np} = 2hf_t/p_n$. Here, h is length of the joint element, and p_n is the normal penalty. In the limit, $\delta_{np} = \lim_{p_n \to +\infty} 2hf_t/p_n = 0$, that is, the critical normal opening amount is close to zero before the normal bonding stress f_t of the joint element is reached. When the normal opening amount reaches δ_{nc}, the joint element breaks and the normal bonding stress decreases to zero. According to the combined single and smear crack model, the relationship between the normal bonding stress and the normal opening amount is given by [17]

$$\sigma = \begin{cases} 2\dfrac{\delta_n}{\delta_{np}}f_t & , \delta_n < 0 \\[2ex] \left[\dfrac{2\delta_n}{\delta_{np}} - \left(\dfrac{\delta_n}{\delta_{np}}\right)^2 \right]f_t & , 0 \leq \delta_n \leq \delta_{np} \\[2ex] zf_t & , \delta_n > \delta_{np} \end{cases} \tag{9}$$

where δ_{nc} is the maximum normal opening amount in which the bonding stress between the joint
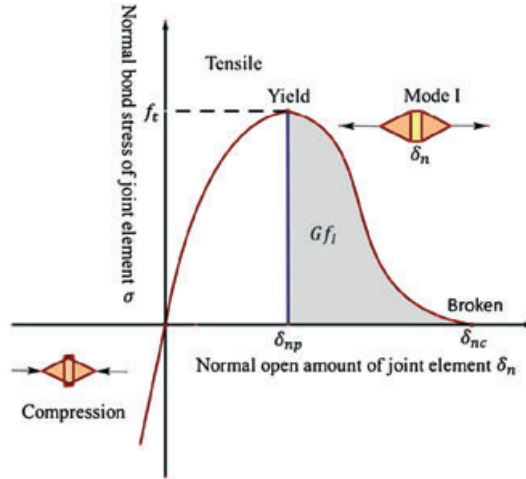
(a) Relationship between normal bond stress and normal open amount
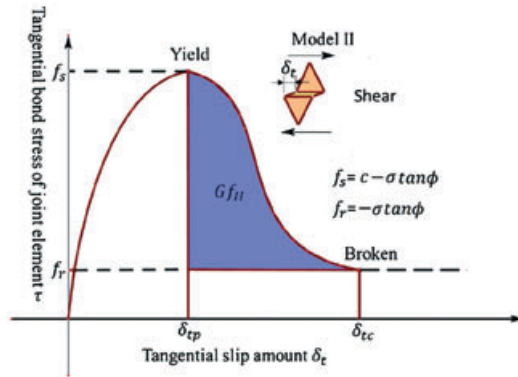
(b) Relationship between tangential bond stress and tangential slip amount

Figure 5. Fracture model of joint elements. (a) Relationship between normal bond stress and normal open amount. (b) Relationship between tangential bond stress and tangential slip amount.

elements is exactly zero, as shown in Figure 5; z is a heuristic softer parameter that can be obtained by fitting experimental stress–strain curves [32], such as

$$z = \left[1 - \frac{a+b-1}{a+b} e^{d(a+cb/((a+b)(1-a-b)))} \right] \times [a(1-d) + b(1-d)^c], \qquad (10)$$

where a, b, and c are constants determined by fitting experimental stress–strain curves; and d is a dimensionless quantity, which represents the opening degree of a joint element

$$d = \begin{cases} 0 & , \delta_n \leq \delta_{np} \\ \dfrac{\delta_n - \delta_{np}}{\delta_{nc} - \delta_{np}} & , \delta_{np} < \delta_n \leq \delta_{nc} . \\ 1 & , \delta_n > \delta_{nc} \end{cases} \qquad (11)$$

If $d = 1$, then the joint element will break; that is, the joint element that connects with two triangular elements will be completely disconnected.

Similarly, the relationship between the tangential bonding stress component and the tangential displacement components (i.e., tangential slip amount) of the joint element is as shown in Figure 5(b).

We mention that Willam *et al.* proposed a more sophisticated interface damage model [26] that satisfies the mechanical dissipation inequality and can be potentially incorporated in the framework of FDEM.

2.4. Time integration to update the coordinate of the triangular element's node

In FDEM, the velocity and displacement of a node are updated in accordance with Newton's second law. The displacement and velocity at each time step are obtained by the finite difference method, as in the following formula:

$$v_i^{(t+\Delta t)} = v_i^{(t)} + \sum F_i^{(t)} \frac{\Delta t}{m_n},$$
$$x_i^{(t+\Delta t)} = x_i^{(t)} + v_i^{(t)} \Delta t \tag{12}$$

where $F_i^{(t)}$ is the resultant force acting at the node , Δt is the time step, and m_n is the node mass, which is equal to one-third mass of a triangular element.

3. POTENTIAL CONTACT FORCE IN FDEM

In FDEM, the potential contact force is adopted for two blocks in contact, one of which is denoted as the contactor β_c and the other as the target β_t, as shown in Figure 6.

The infinitesimal contact force of a differential area dA in the overlapping area $\beta_c \cap \beta_t$ at point $P \in \beta_c \cap \beta_t$ is denoted by d$\mathbf{f}_c$, reading

$$d\mathbf{f}_c = p_n[\text{grad}\,\phi_c(P) - \text{grad}\,\phi_t(P)], \tag{13}$$

Here, φ_c and φ_t are the potential functions with regard to β_c and β_t, respectively; p_n is the penalty. Integrating $d\mathbf{f}_c$ over $\beta_c \cap \beta_t$ and applying Green's theorem, we have the total potential contact force

$$\mathbf{f}_c = p_n \int_{\Gamma_{\beta_c \cap \beta_t}} [\phi_c(P) - \phi_t(P)] \mathbf{n} dS, \tag{14}$$

which is exerted on β_c by β_t. Here, $\mathbf{n}$ represents the outward unit normal vector, and $\Gamma_{\beta_c \cap \beta_t}$ is the boundary of $\beta_c \cap \beta_t$.

Now, let us return the situation of two triangular solid elements in contact. To ensure the work carried out by the contact force is zero, Munjiza showed that the potential along the boundaries of two elements in contact should be constant. Based on this, the potential function is defined as [13]

$$\varphi(P) = \min\left\{\frac{3A_1}{A}, \frac{3A_2}{A}, \frac{3A_3}{A}\right\}, \tag{15}$$

where A_i ($i = 1, 2, 3$) is area of the sub-triangle composed by point P and one of the three sides of the triangular element, and A is area of the triangular element, as shown in Figure 7.
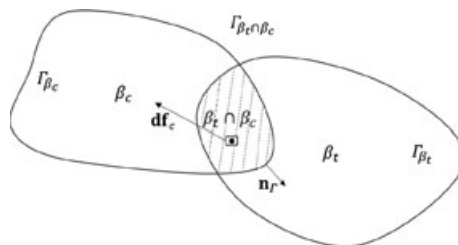

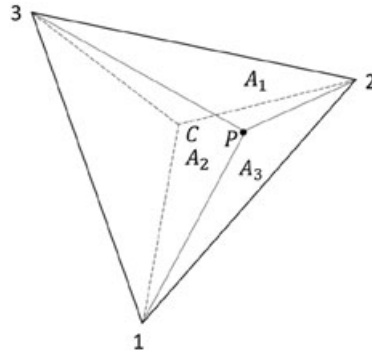Figure 6. Schematic of potential contact force calculation.

Figure 7. Potential of point P within a triangle.

Obviously, the potential of the center C of a triangle is equal to 1, but on the boundary of the triangle, the potential is equal to zero. In order to understand easily, a triangle can be divided into three sub-triangles by the center C and three sides of the triangle, as shown in Figure 7. Then, if we want to obtain the potential of a point, we firstly need to determine in which sub-triangle the point is located. For example, assuming point P is located in the sub-triangle $C12$, according to Equation (15), the potential of point P can be rewritten as

$$\varphi(P) = \frac{3A_3}{A} = \frac{h_{p-12}}{\frac{1}{3}h_{3-12}},$$
(16)

where h_{p-12} represents the distance from point P to edge 12, that is, the height of the triangle on that edge.

Although the potential function defined in Equation (15) satisfies that the potential on the boundary is constant, the physical meaning of the potential is not clear. For example, the contact force based on the original potential function is different even if the embedding amount is the same. A brief analysis of the potential function is conducted as follows.

Shown in Figure 8 are two pairs of contact elements, where the size of the contactor element is different, but both the target elements are exactly the same, and the edge labeled L of contactor element is parallel to the edge labeled 12 and $1'2'$ of the target element, with an equal distance. According to Equations (14) and (16), the potential contact force exerted on the edge L by the target element in the left contact pair is given by

$$\mathbf{f}_c = p_n \int_L \mathbf{n}_L (0 - \varphi_t) dL = -\mathbf{n}_L p_n \int_L \frac{3h_{p-12}}{h_{3-12}} dL = -\mathbf{n}_L p_n \frac{3h_{p-12}}{h_{3-12}} L.$$
(17)

Here, $\mathbf{n}_L$ is outward normal vector of the edge L; h_{p-12} is distance between edges L and 12, and h_{3-12} is distance from node 3 to edge 12.
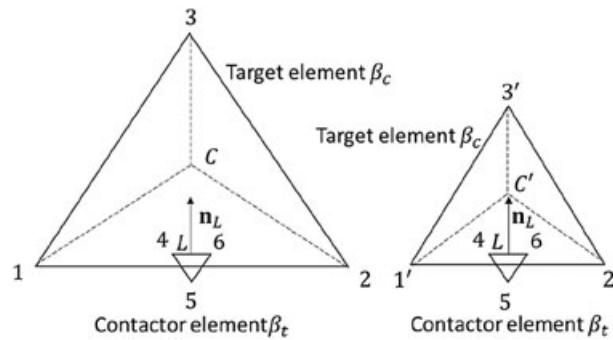

Figure 8. Two contact pairs with same embedded amount.

Similarly, the contact force exerted on the edge L by the target element in the right contact pair can be obtained as

$$\mathbf{f}_{c'} = p_n \int_L \mathbf{n}_L (0 - \varphi_t) \mathrm{d}L = -\mathbf{n}_L p_n \int_L \frac{3h_{p-1'2'}}{h_{3'-1'2'}} \mathrm{d}L = -\mathbf{n}_L p_n \frac{3h_{p-1'2'}}{h_{3'-1'2'}} L. \tag{18}$$

However, $h_{3-12} > h_{3'-1'2'}$ even though $h_{p-12} = h_{p'-1'2'}$, leads to $f_c < f_{c'}$. This indicates that although the embedded amount is the same, the contact force is not equal but dependent on the size of two triangular elements in contact.

Here, only one boundary of the overlapping zone is analyzed. To obtain the total contact force, we need to integrate over all the boundaries of the overlapping zone. Similar to the aforementioned analysis, for the two contact pairs as shown in Figure 8, the total contact force based on the original potential function is shown in Table I (the penalty p_n is 67.3 GPa, and the total contact force has been assigned to the nodes of the contactor element). However, the total contact forces in Table I are different even though the embedded amount of the two contact pairs are equal, which indicates that the contact force is dependent upon the mesh. For this reason, we propose a new potential function based on a unified standard in the next section. The contact force given by this new potential function will be equal as long as the embedding amount is the same. Thus, the potential can characterize the embedding amount based on a unified standard.

4. NEW POTENTIAL FUNCTION BASED ON UNIFIED STANDARD

4.1. Basic idea

In order to solve the problems of the original potential function, a new potential function is defined to ensure that the potential characterizes embedded amount, where the potential of a point within a triangle is proportional to the shortest distance from the point to the three sides of the triangle. The new potential function is given by

$$\varphi(P) = k\min\{h_{p-12}, h_{p-23}, h_{p-31}\}, \tag{19}$$

where k is a proportional constant; and h_{p-12}, h_{p-23}, and h_{p-31} are the distance from point P to the three sides (edges 12, 23, and 31) of the triangle, respectively, as shown in Figure 9.

To make the potential characterize the embedded amount based on a unified standard and ensure the potential is dimensionless, we define a standard length H. When the embedded amount of one point is equal to H, the potential of the point is 1. By setting $k = 1/H$ in Equation (19), the new potential function can be written as

$$\varphi(P) = \frac{1}{H}\min\{h_{p-31}, h_{p-12}, h_{p-23}\}, \tag{20}$$

where H is the standard embedded amount. One-third of the minimum height of all the triangular elements is taken as the value of H to avoid excessive embedding.

Now let us make a further analysis to Equation (20). As shown in Figure 9, the triangle is divided into three sub-triangles by the incenter and three sides of the triangle. To obtain the potential of a

Table I. Contact force calculated based on the original potential function.

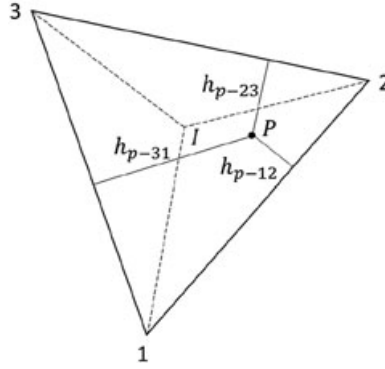| | Element node ID | | | | | |
| | 4 | | 5 | | 6 | |
| | | | Node force (GN) | | | |
	fx	fy	fx	fy	fx	fy
Left contact pair	0.7478	−8.8487	0.0000	−5.8576	−0.7478	−8.8487
Right contact pair	1.1217	−10.2819	0.0000	−5.7953	−1.1217	−10.2819

Figure 9. Potential ϕ at point P based on the new potential function.

point, we firstly determine which sub-triangular contains the point. Assuming point P is in the sub-triangle $I12$, according to Equation (20), the potential of point P can be written as

$$\varphi(P) = \frac{1}{H} h_{p-12}. \tag{21}$$

Therefore, a point where the potential reaches the maximum must be the incenter of the triangle. However, the potential of that point is not necessarily equal to 1, and the potential of incenters in different triangles may be different. This is different from Munjiza's potential function, where the potential is the maximum at the center point of a triangle, and the potential of the center point in different triangle is always equal to 1. By comparing Equations (16) and (21), we find that only the denominator is different: the denominator in Munjiza's potential function is $h_{3-12}/3$, while in the new function, the denominator is H. The value of h_{3-12} will vary with the shape of the triangle, but the value H is an invariant. Thus, the new potential function characterizes the embedded amount based on a unified standard for all the triangular solid elements in the mesh. Using the new potential function, we can obtain the same contact force for the same embedding amount. As a consequence, the physical meaning of the potential becomes clear and independent of the two contact elements. At the same time, the new potential on the boundary is also zero, satisfying the condition that the potential on the boundary should be constant.

We still use Figure 8 as an example. According to Equations (14) and (21), the contact force of the target element on the edge L of the contactor element is

$$\mathbf{f}_c = p_n \int_L \mathbf{n}_L (0 - \varphi_t) dL = -\mathbf{n}_L p_n \int_L \frac{h_{p-12}}{H} dL = -\mathbf{n}_L p_n \frac{h_{p-12}}{H} L. \tag{22}$$

As the embedding amount is equal, that is, $h_{p-12} = h_{p-1' \cdot 2'}$, according to Equation (22), the total contact force for the two contact pairs in Figure 8 is the same. This can be demonstrated by example 1 of Section 5.

4.2. Implementation in programming

As discussed in Section 4.1, what we have done is just to redefine a new potential function. In the original potential function, the triangle is divided into three sub-triangles with the center point of the triangle as one common vertex of the three sub-triangles, as shown in Figure 7. However, in the new potential function, the triangle is divided into three sub-triangles with the incenter of the triangle as one common vertex of the three sub-triangles, as shown in Figure 10. $I2$ is a line segment connecting node 2 and incenter I of the target element. As the potential at edge AB is a piecewise linear function, which turns at the intersection P_1 of edge AB and the line segment $I2$. Using the new potential function, we just need to replace the center point C of the triangle in Figure 7 by the incenter I of the triangle to find the two intersection of P_1 and P_2 and use Equation
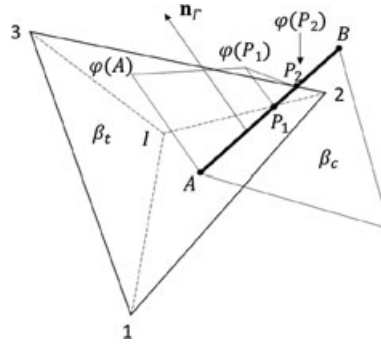
Figure 10. Contact force of target element β_t on the edge AB of contactor element β_c.

(20) to calculate the potential on edge AB. Obviously, the modification is easy to implement, with a minor change to the original code.

Having obtained the intersections P_1 of edge AB with angle bisector $I2$ and P_2 of edge AB with edge 23, we calculate the contact force of the target element β_t on edge AB of contactor element β_t according to Equation (14):

$$\mathbf{f}_c = p_n \int_{l_{AB}} \mathbf{n}_\Gamma (0 - \varphi_t) \mathrm{d}l = -\mathbf{n}_\Gamma p_n \int_{l_{AB}} \varphi_t \mathrm{d}l. \tag{23}$$

As the distribution of potential ϕ_t on edge AB is a piecewise linear function, the value of $\int_{l_{AB}} \phi_t \mathrm{d}l$ is equal to area of the zone as shown in Figure 10. Thus, Equation (23) can be further written as

$$\mathbf{f}_c = -\mathbf{n}_\Gamma p_n \frac{1}{2} \left((\varphi_t(A) + \varphi_t(P_1)) l_{AP_1} + (\varphi_t(P_1) + \varphi_t(P_2)) l_{P_1 P_2} \right). \tag{24}$$

Here, according to Equations (20) and (21), we have

$$\varphi_t(A) = \frac{h_{A-12}}{H}, \varphi_t(P_1) = \frac{h_{P_1-12}}{H}, \varphi_t(P_2) = \frac{h_{P_2-23}}{H} = 0. \tag{25}$$

5. EXAMPLES

5.1. Example 1

For the example as shown in Figure 8, we calculate the total contact force based on the new potential function, and the normal penalty p_n is still 67.3 GPa as in Section 3. The contact force of the two contact pairs is reported in Table II (contact force has been assigned to the nodes of contactor element). Table II shows that the contact force is exactly the same for the two contact pairs when the new potential function is used.

Table II. Contact force based on the new potential function.

	Element node ID					
	4		5		6	
			Node force (GN)			
	fx	fy	fx	fy	fx	fy
Left contact pair	3.5893	−17.7411	0.0000	−3.3838	−3.5893	−17.7411
Right contact pair	3.5893	−17.7411	0.0000	−3.3838	−3.5893	−17.7411

5.2. Example 2

The example as shown in Figure 8 is a rather particular case and makes it easy to make a theoretical analysis. However, that example cannot fully reflect the advantages of the new potential function and cannot completely expose why the original potential function is not very unreasonable.

As shown in Figure 11, keeping the overlap zone of the contact pair unchanged, if we replace edge AB by $A'B$ or replace CD by CD', the total contact force based on the original potential function will change, contrary to the common sense. The correct result is that the contact force should be equal as long as the overlap zone of the contact pair keeps unchanged. For instance, as shown in Figure 12, no matter how the third edge of the contact triangle elements changed, the contact force should be equal as long as the overlapping zone is the same, which can be exactly reflected by the new potential function. Thus, the defects of the original potential function have been overcome.

To verify the aforementioned discussion, we calculated the total contact force of the four contact pairs in Figure 11, namely, ABE and CDF, ABE and $CD'F$, $A'BE$ and CDF, and $A'BE$ and $CD'F$, using the original potential function and the new potential function, respectively. As the shape of the triangular element is changed, the contact force assigned to each node of the contactor element is also different. Thus, we only compare the total contact forces acting on the contactor element; the results are reported in Table III. Table III shows that the total contact force based on the original potential function is different, but the contact force based on the new potential function is exactly the same.
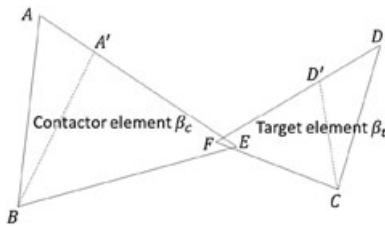

Figure 11. Four contact pairs with the same embedded amount.
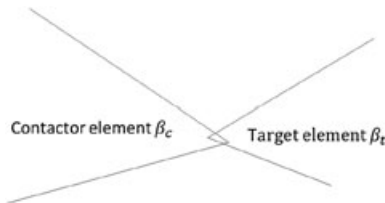

Figure 12. Generalization of contact pairs with the same embedded amount.

Table III. Comparison of contact forces based on the original and new potential function.

| | Total contact force (GN) | | | |
| | New potential function | | Original potential function | |
	fx	fy	fx	fy
ABE with CDF	−2.5203	−2.6394	−1.3006	−1.3907
ABE with $CD'F$	−2.5203	−2.6394	−1.5822	−1.6908
$A'BE$ with CDF	−2.5203	−2.6394	−1.3491	−1.5165
$A'BE$ with $CD'F$	−2.5203	−2.6394	−1.6306	−1.8166

5.3. Example 3

In this section, a slope slider example having analytical solution is used to illustrate the difference of contact forces based on the original and new potential functions. As shown in Figure 13, a slider is placed on the slope with an angle of $\theta = 45°$, the height of the slope is $10\,\text{m}$, the inclined plane is smooth, the area of the slider is $5.656854\,\text{m}^2$, density $\rho = 2650\,\text{kg/m}^3$, and gravitational acceleration $g = 9.8\,\text{m/s}^2$.

In order to expose the defects of the original potential function clearly, we use an extreme mesh to discretize the slope, as shown in Figure 13. As the inclined plane is smooth, the slider only bears the normal contact force. The analytical solution of the contact force is $F_N = mg\cos\theta = 1.03880 \times 10^5\,\text{N}$. The original and new potential functions in FDEM are used to analyze this example, respectively. The time history curve of the total contact force is shown in Figure 14.

It can be seen from Figure 14(a) and (b) that the contact force from the new potential function converges to the analytical solution faster than that from the original potential function. After that, the contact forces from the two potential functions do not display obvious difference, and the curves of contact force versus time are almost coincident. However, from Figure 14(c), we can find that the contact force from the new potential function keeps unchanged and always equals to the analytical solution, but the curve of the contact force versus time from the original potential function has five oscillations after $t = 0.05\,\text{s}$. The cause of oscillation is that the elements of the slope in contact with the slider are quite different in both shape and size as the slider moves down. Therefore, the contact force from the original potential function has mesh dependence. But the contact force from the new potential function does not have this problem. When the mesh of the contact zone changes, the contact force from the new potential function remains unchanged. This indicates that the contact force from the new potential function is mesh independent.

Figure 15 shows the slider position at the time $t = 1.541013\,\text{s}$, where the slider displacement is $8.228\,\text{m}$, which is consistent with the analytical solution.

Now, we calculate the time when the five oscillations occur. As shown in Figure 16, the spacing L of the mesh along the inclined plane is $1.414214\,\text{m}$. This means that as long as the slider slide moves L distance along the inclined plane, the element of the slope in contact with the slider will change. According to the analytical solution of the slider displacement $s = \frac{1}{2}g\sin(\theta)t^2$, when $s = L$, $2L$, $3L$, $4L$, and $5L$, the element of the slope changes at $t = 0.6389$, 0.9035, 1.1066, 1.2778, and $1.4286\,\text{s}$, coinciding with the time moments shown in Figure 14(c) when oscillations occur. This further illustrates that the contact force from the original potential function is closely related to the mesh of the contact zone.

5.4. Example 4

Examples 1 to 3 aim only to validate and compare the contact forces derived from the two potential functions. In this section, a Brazilian disc example is designed to demonstrate the full advantages of the new potential function and the difference between the two potential functions.

As shown in Figure 17, two different meshes are used. The mesh in Figure 17(a) is uniform with each triangle approximately equal equilateral, and the mesh in Figure 17(b) has quite different
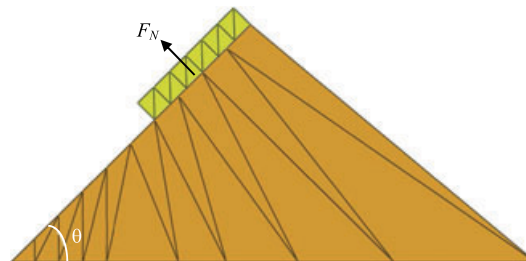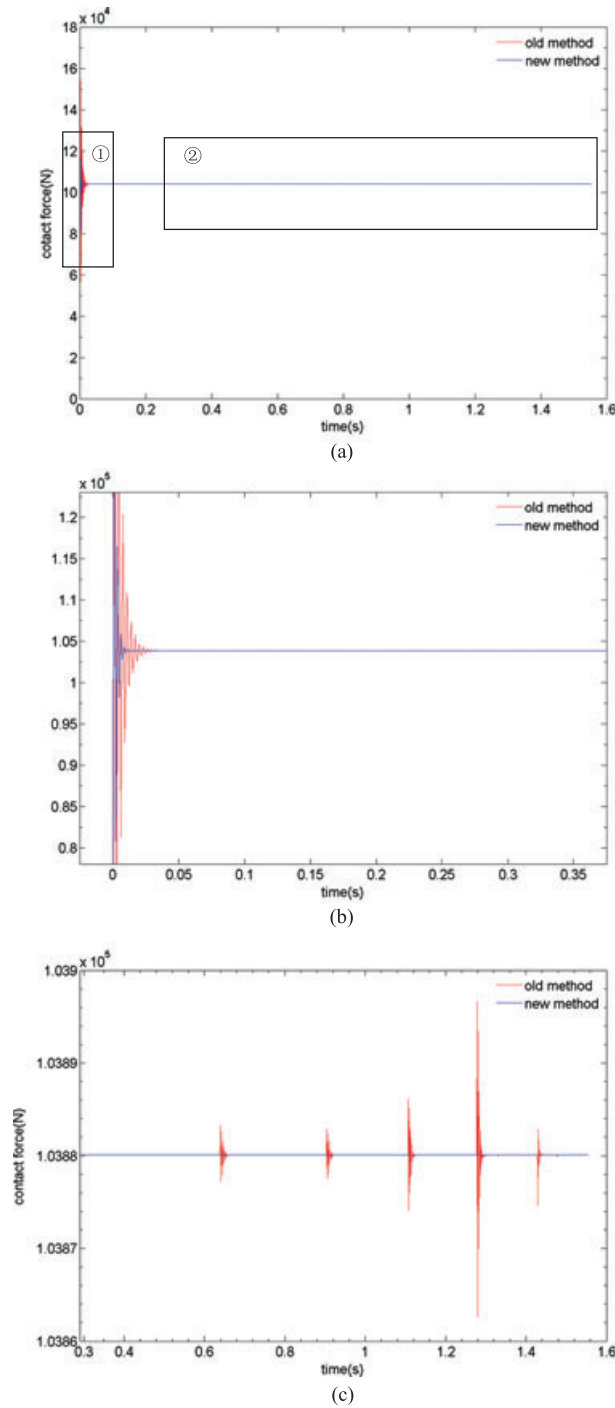

Figure 13. The mesh configuration of example 3.

Figure 14. Contact force of slider versus time: (a) contact force of slider versus time, (b) locally enlarged view (rectangular box ① in (a)) of the contact force–time curve, and (c) locally enlarged view (rectangular box ② in (a)) of the contact force–time curve.

triangular elements in size. With the two meshes, we trace the crack paths using the original and new potential functions in FDEM, respectively. The simulation results are shown in Figures 18 and 19.

As shown in Figure 18, when the uniform mesh (Figure 17(a)) is used, the crack morphology obtained by the two potential function is basically the same. This is because the triangular elements are approximately equal equilateral triangle and the center point of a triangular element almost
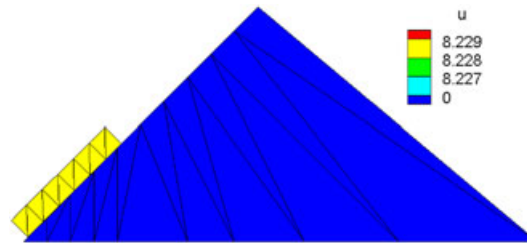
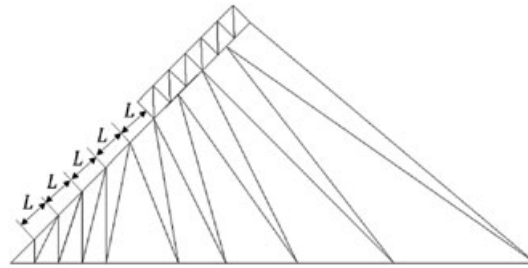Figure 15. When $t = 1.541013$ s, the position of slider on the slope.

Figure 16. The spacing along the inclined plane ($L = 1.414214$ m).
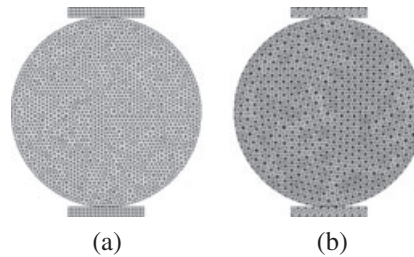

(a)   (b)

Figure 17. Two different meshes: (a) uniform (all elements are approximately equal equilateral triangle) and (b) non-uniform (element sizes are quite different).

coincides with the incenter of the triangular element. Thus, the two potential functions are the same in essence.

However, when non-uniform mesh (Figure 17(b)) is used, as shown in Figure 19, the crack paths derived from the two potential functions are not consistent. The crack by the new potential function propagates along the vertical diameter of the disc basically, which is close to the theoretical analysis, and the distribution of stress is more uniform than that by the original potential function. Nevertheless, the major crack path by the original potential function deviates from the vertical diameter of the disk, and many branch cracks emerge at the upper and bottom of the disc. This is because the contact force derived from the original potential function is unevenly distributed. As a conclusion, even when a dense mesh is used, the crack path from the original potential function may deviate far from the theoretical solution. Instead, when the new potential function is used, the crack path is closer to the theoretical solution as the mesh density increases. This indicates that the new potential function has less mesh dependence in the simulation of crack propagation.

Figure 20 is the load–displacement curves by both the potential functions. Although there is some difference in the peak strength, the difference between the two potential functions is not obvious as a whole. Here is an explanation for this. The load–displacement curve of a rock sample is controlled by its strength and deformation properties. The most important thing in the simulation of cracking is to maintain the satisfaction of the momentum conservation law. The FDEM based on either the original potential function or the new potential function just obeys the momentum conservation law.
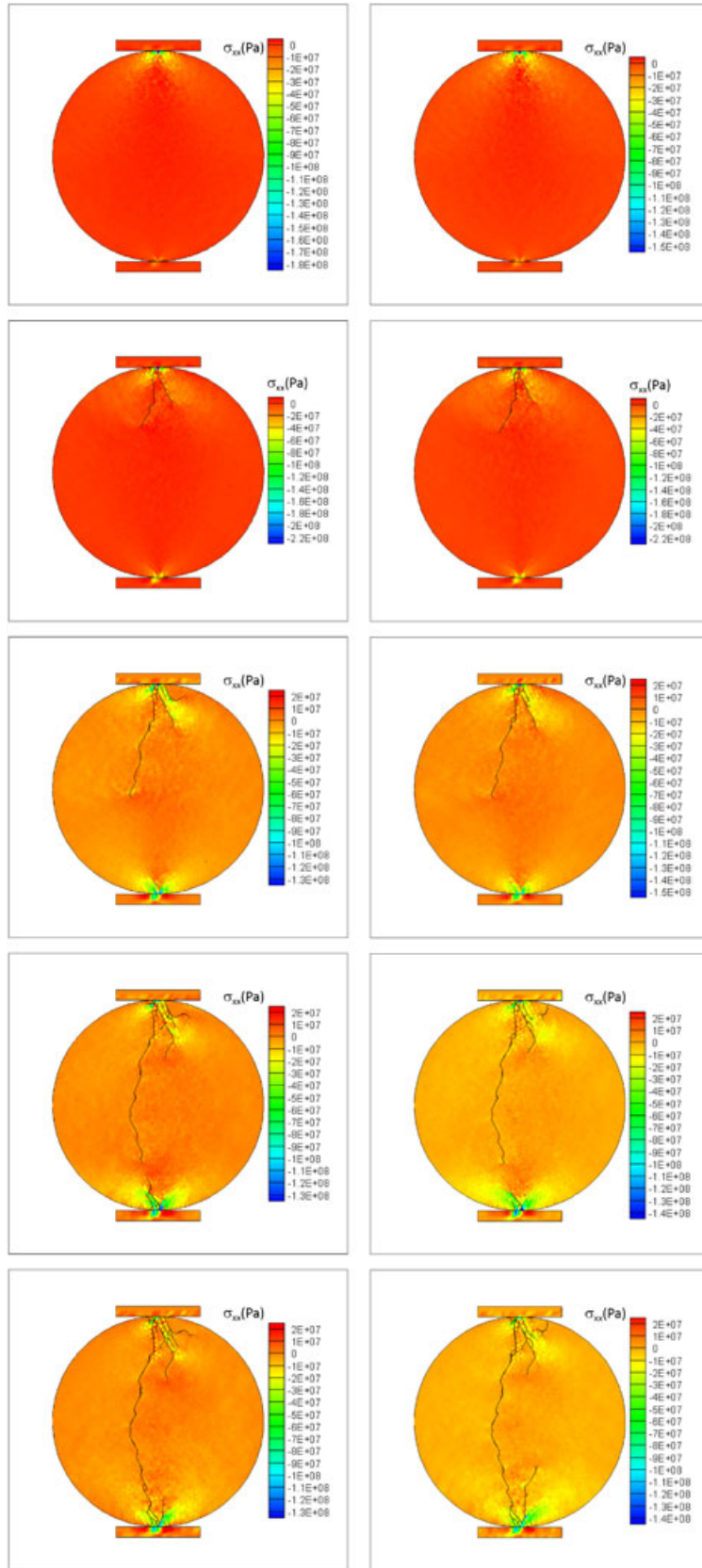
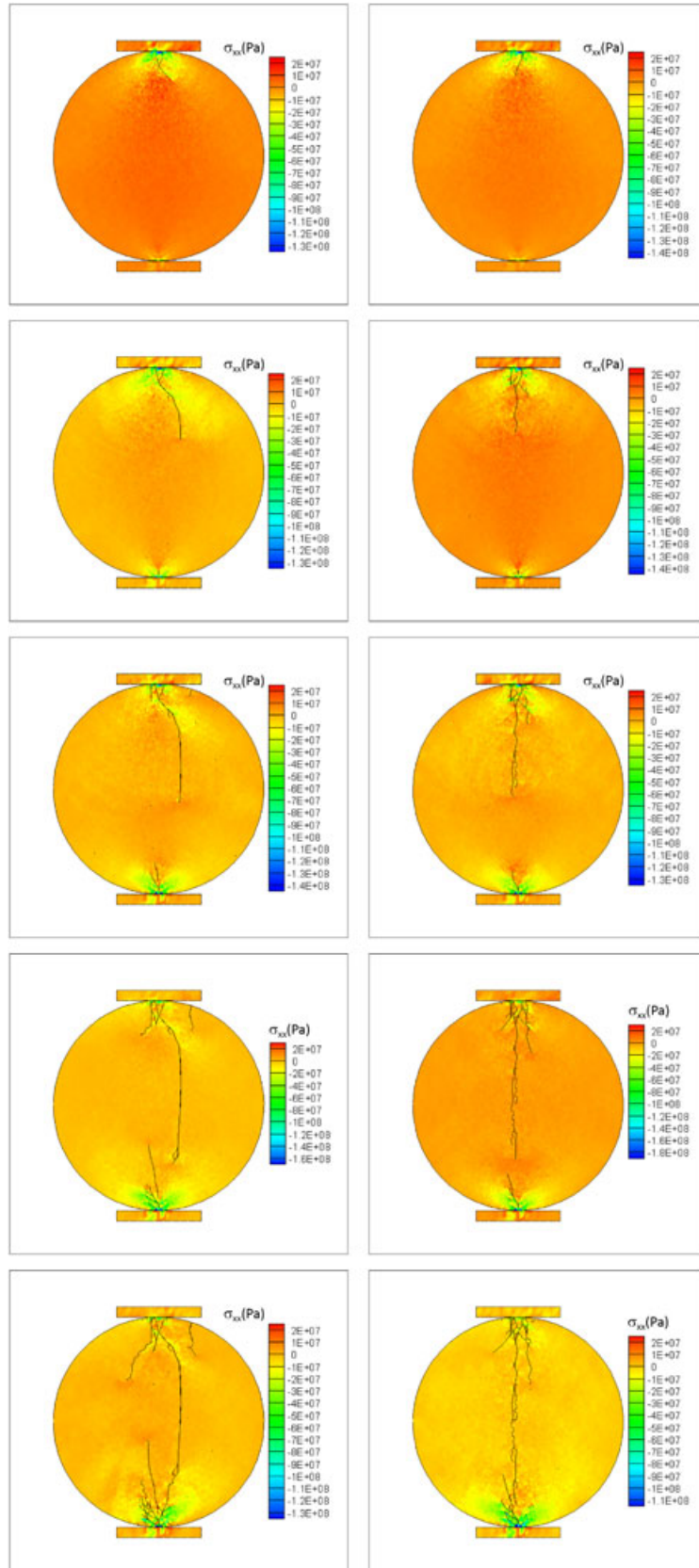Figure 18. Comparison of results from the two potential functions (uniform mesh).

Figure 19. Comparison of results from the two potential functions (non-uniform mesh).
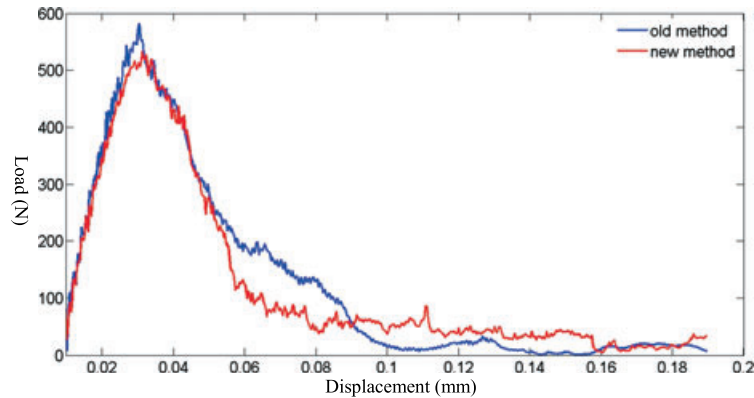
Figure 20. Load–displacement curves of the Brazilian disc tests.

6. CONCLUSION

In this study, a new potential function is proposed. With this new potential function, for the same embedded amount, the contact force is equal. Moreover, it preserves all the advantages of the original potential function. The following conclusions can be drawn:

1. Some defects of the original potential function was pointed out; for example, the physical meaning of the original function is not clear; the contact force derived from the original function does not match the physical intuition and has a rather strong dependency on the mesh configuration.
2. The new potential of a point within a triangular element is proportional to the distance of the point to the triangular element boundary; the maximum potential is not always equal to one; and the potentials of the incenters in different triangular elements are not necessarily equal.
3. The new potential function characterizes the embedded amount, with a clearer physical meaning but less mesh dependency.
4. The crack paths derived from the new potential function appear to be in better agreement with the analytical results.

REFERENCES

1. Sagong M, Bobet A. Coalescence of multiple flaws in a rock-model material in uniaxial compression. *International Journal of Rock Mechanics and Mining Sciences* 2002; **39**(2):229–241.
2. Yang SQ, Liu XR, Jing HW. Experimental investigation on fracture coalescence behavior of red sandstone containing two unparallel fissures under uniaxial compression. *International Journal of Rock Mechanics and Mining Sciences* 2013; **63**:82–92.
3. Bobet A. The initiation of secondary cracks in compression. *Engineering Fracture Mechanics* 2000; **66**(2):187–219.
4. Wong RHC, Chau KT, Tang CA, Lin P. Analysis of crack coalescence in rock-like materials containing three flaws —part I: experimental approach. *International Journal of Rock Mechanics and Mining Sciences* 2001; **38** (7):909–924.
5. Liang ZZ, Tang CA, Li HX, Xu T, Zhang YB. Numerical simulation of 3-d failure process in heterogeneous rocks. *International Journal of Rock Mechanics and Mining Sciences* 2004; **41**(3):323–328.
6. Horii H, Nemat-Nasser S. Brittle failure in compression: splitting, faulting and brittle-ductile transition. *Philosophical Transactions of the Royal Society of London A: Mathematical, Physical and Engineering Sciences* 1986; **319** (1549):337–374.
7. Zheng H, Liu F, Li CG. The MLS-based numerical manifold method with applications to crack analysis. *International Journal of Fracture* 2014; **190**(1):47–166.
8. Zheng H, Liu F, Du XL. Complementarity problem arising from static growth of multiple cracks and MLS-based numerical manifold method. *Computer Methods in Applied Mechanics and Engineering* 2015; **295**:150–171.

9. Tang CA, Kou SQ. Crack propagation and coalescence in brittle materials under compression. *Engineering Fracture Mechanics* 1998; **61**(3):311–324.
10. Tang CA, Yang WT, Fu YF, Xu XH. A new approach to numerical method of modelling geological processes and rock engineering problems—continuum to discontinuum and linearity to nonlinearity. *Engineering Geology* 1998; **49**(3):207–214.
11. Liang ZZ, Xing H, Wang SY, Williams DJ, Tang CA. A three-dimensional numerical investigation of the fracture of rock specimens containing a pre-existing surface flaw. *Computers and Geotechnics* 2012; **45**:19–33.
12. Potyondy DO, Cundall PA. A bonded-particle model for rock. *International Journal of Rock Mechanics and Mining Sciences* 2004; **41**(8):1329–1364.
13. Munjiza A. *The Combined Finite–Discrete Element Method*. Wiley: London, 2004.
14. Munjiza A, Knight E, Rougier E. *Computational Mechanics of Discontinua*. Wiley: London, 2012.
15. Mahabadi OK, Lisjak A, Munjiza A, Grasselli G. Y-Geo: new combined finite–discrete element numerical code for geomechanical applications. *International Journal of Geomechanics* 2012; **12**(6):676–688.
16. Mahabadi OK, Grasselli G, Munjiza A. Y-GUI: a graphical user interface and pre-processor for the combined finite–discrete element code, Y2D, incorporating material heterogeneity. *Computers & Geosciences* 2010; **36**(2):241–252.
17. Munjiza A, Andrews KRF, White JK. Combined single and smeared crack model in combined finite–discrete element analysis. *International Journal for Numerical Methods in Engineering* 1999; **44**(1):41–57.
18. Munjiza A, Andrews KRF. Penalty function method for combined finite–discrete element systems comprising large number of separate bodies. *International Journal for Numerical Methods in Engineering* 2000; **49**(11):1377–1396.
19. Cundall PA. A computer model for simulating progressive large scale movements in blocky rock systems. *Proceedings of the International Symposium on Rock Fracture*, Nancy, 1971.
20. ITASCA Consulting Group, Inc. User manual of UDEC code, 2005.
21. Lankarani HM, Nikravesh PE. A contact force model with hysteresis damping for impact analysis of multibody systems. *Journal of Mechanical Design* 1990; **112**(3):369–376.
22. Elata D, Berryman JG. Contact force–displacement laws and the mechanical behavior of random packs of identical spheres. *Mechanics of Materials* 1996; **24**(3):229–240.
23. Di Renzo A, Di Maio FP. Comparison of contact-force models for the simulation of collisions in DEM-based granular flow codes. *Chemical Engineering Science* 2004; **59**(3):525–541.
24. Choi J, Rhim S, Choi JH. A general purpose contact algorithm using a compliance contact force model for rigid and flexible bodies of complex geometry. *International Journal of Non-Linear Mechanics* 2013; **53**:13–23.
25. Wang FJ, Wang LP, Cheng JG, *et al.* Contact force algorithm in explicit transient analysis using finite-element method. *Finite Elements in Analysis and Design* 2007; **43**(6):580–587.
26. Willam K, Rhee I, Shing B. Interface damage model for thermomechanical degradation of heterogeneous materials. *computer Methods in Applied Mechanics and Engineering* 2004; **193**:3327–3350.
27. Aballero A, Willam K, Carol I. Consistent tangent formulation for 3D interface modelling of cracking/fracture in quasi-brittle materials. *Computer Methods in Applied Mechanics and Engineering* 2008; **197**:2804–2822.
28. Xuan Z, Papadopoulos P, Li J, *et al.* An entropy-based evaluation of contact forces in continuum mechanics of elastic structures. *Finite Elements in Analysis and Design* 2016; **114**:78–84.
29. Munjiza A, Andrews KRF. NBS contact detection algorithm for bodies of similar size. *International Journal for Numerical Methods in Engineering* 1998; **43**(1):131–149.
30. Munjiza A, Rougier E, John NWM. MR linear contact detection algorithm. *International Journal for Numerical Methods in Engineering* 2006; **66**(1):46–71.
31. Munjiza A, Knight EE, Rougier E. *Large Strain Finite Element Method: A Practical Course*. John Wiley & Sons: London, 2015.
32. Evans RH, Marathe MS. Microcracking and stress–strain curves for concrete in tension. *Materials and Structures* 1968; **1**(1):61–64.